



# Learning-Based Cell Injection Control for Precise Drop-on-Demand Cell Printing

JIA SHI<sup>1,2</sup>, BIN WU,<sup>2</sup> BIN SONG,<sup>3</sup> JINCHUN SONG,<sup>1</sup> SHIHAO LI,<sup>4</sup> DIETER TRAU,<sup>4</sup> and WEN F. LU<sup>2</sup>

<sup>1</sup>School of Mechanical Engineering and Automation, Northeastern University, Shenyang, Liaoning, China; <sup>2</sup>Department of Mechanical Engineering, National University of Singapore, 9 Engineering Drive 1, Singapore 1197576, Singapore; <sup>3</sup>Singapore Institute of Manufacturing Technology, Singapore, Singapore; and <sup>4</sup>Department of Biomedical Engineering, National University of Singapore, Singapore, Singapore

(Received 14 February 2018; accepted 16 May 2018; published online 5 June 2018)

Associate Editor Smadar Cohen oversaw the review of this article.

**Abstract**—Drop-on-demand (DOD) printing is widely used in bioprinting for tissue engineering because of little damage to cell viability and cost-effectiveness. However, satellite droplets may be generated during printing, deviating cells from the desired position and affecting printing position accuracy. Current control on cell injection in DOD printing is primarily based on trial-and-error process, which is time-consuming and inflexible. In this paper, a novel machine learning technology based on Learning-based Cell Injection Control (LCIC) approach is demonstrated for effective DOD printing control while eliminating satellite droplets automatically. The LCIC approach includes a specific computational fluid dynamics (CFD) simulation model of piezoelectric DOD print-head considering inverse piezoelectric effect, which is used instead of repetitive experiments to collect data, and a multilayer perceptron (MLP) network trained by simulation data based on artificial neural network algorithm, using the well-known classification performance of MLP to optimize DOD printing parameters automatically. The test accuracy of the LCIC method was 90%. With the validation of LCIC method by experiments, satellite droplets from piezoelectric DOD printing are reduced significantly, improving the printing efficiency drastically to satisfy requirements of manufacturing precision for printing complex artificial tissues. The LCIC method can be further used to optimize the structure of DOD print-head and cell behaviors.

**Keywords**—Cell printing, Machine learning, Artificial neural network, Multilayer perceptron, Computational fluid dynamics.

## INTRODUCTION

DOD cell printing provides a high resolution and throughput with little damage to cell viability that makes it widely used in bioprinting for tissue engineering, such as printing full tissue regeneration.<sup>1,2,11</sup> For instance, intestinal wall is composed of epithelial cells, connective cells and muscle cells in specified arrays. Different cells are separated by precise micro boundaries (Fig. 1(a)). As the nozzle of DOD print-head is small, usually less than 120  $\mu\text{m}$ , DOD printing is suitable for manufacturing the micro boundary of cells.<sup>15</sup> Controlled positioning cells is important in tissue engineering because the various cell types in organs are not randomly mixed but specifically arranged according to the needs and functions. Also, the position of cells on the scaffold has to be controlled for the detection of stress experienced by cells and response to external mechanical forces.<sup>26</sup> Ideally, a primary droplet without satellite droplets should be created during DOD printing with precise cells position (Fig. 1(b)). However, as shown in Fig. 1(c), if unsuitable printing parameters were used, satellite droplets could be produced together with the primary droplet, leading to cells splash, disordered cells arrays and further structure errors. Xu and Zhang<sup>28</sup> analyzed the influence of cell concentration on satellite droplets formation and the movement trace. They found that satellite droplets were suppressed with the increase of cell concentration. Xu and Chai<sup>27</sup> also found that the best printing performance was printing only primary droplet. This printing performance has the best position accuracy and feature resolution.

Currently, DOD printing relies on the empirical adjustment of printing parameters to avoid generation

Address correspondence to Wen F. Lu, Department of Mechanical Engineering, National University of Singapore, 9 Engineering Drive 1, Singapore 1197576, Singapore. Electronic mail: mpelwf@nus.edu.sg

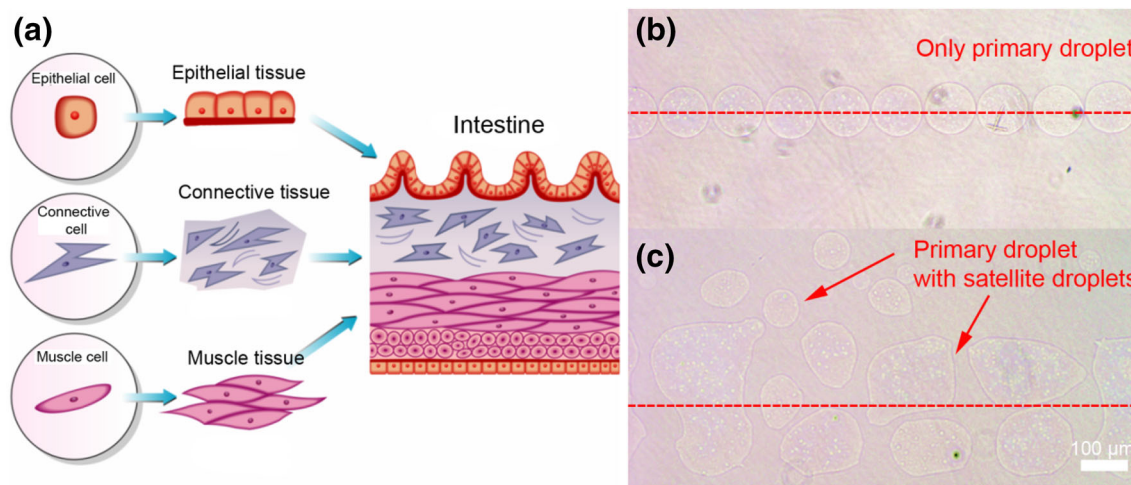


**FIGURE 1.** Ideal printed tissues by DOD cell printing and actual droplets generated on the substrate. (a) Schematic of intestinal wall; (b) Only primary droplet printed; (c) Primary and satellite droplets printed. Dash line is the planning route.

of satellite droplets.<sup>27</sup> Such way of adjustment is difficult to achieve reliable results with desirable precision because different printing parameters are required with different viscosities and surface tensions of different bio-inks. Thus, the time-consuming trial-and-error process is normally used to figure out the optimal parameters for different bio-inks to prevent satellite droplets generation.

CFD simulations have made a great contribution to 3D printing process by analyzing the influence of each printing parameter on droplet volume and speed. However, formation and elimination of satellite droplets were rarely studied because of the coupling effect of printing parameters, which makes it difficult to develop a good mathematical model.<sup>13,23</sup> Carrying out a number of CFD simulations before an experiment was also unrealistic due to its large computational time and high expense.

One promising approach is to use machine learning to solve these complex issues by focusing on the relationships between parameter datasets. Artificial neural network (ANN) is one of well-established machine learning methods, which simulates the process of human learning. It can self-study the relation and rule of given dataset. Thus it is popular in data classification<sup>5,12</sup> and prediction based on the classification model due to its power, flexible, and relatively easy operations. Currently, ANN has been applied widely for optimal control scheme<sup>22</sup> and classification.<sup>5</sup> For instance, it was used to solve variable classification problems in bioengineering, such as biodegradation,<sup>8</sup> bioprocess design,<sup>6</sup> and anthological analysis.<sup>30</sup> ANN was also used to design scaffolds for tissue engineering. Notably, Vatankhah<sup>25</sup> used ANN to optimize electrospun scaffolds for tissue engineering. The influence of polymeric composition, fibre diameter and fibre

orientation of electrospun polycaprolactone on the elastic modulus of scaffolds were investigated. With the relation learnt by ANN, datasets under the same condition can be automatically classified. For instance, in our work, ANN can help to separate droplets into three categories: 'no droplet', 'single primary droplet' and 'satellite droplets'. Satellite droplets can be predicted with specific input parameters accordingly.

A class of ANNs is Multilayer Perceptron (MLP). Santos<sup>7</sup> used multilayer perceptron (MLP) to analyze droplet speed in pulsed gas metal arc welding. 30 droplet speeds measured in the experiment were used as the training set. Six random droplet speeds were used to test the accuracy. Test droplet speeds are from 0 to  $2.5 \text{ m s}^{-1}$  within a margin of error of  $\pm 0.33 \text{ m s}^{-1}$ . They showed a satisfactory performance of the MLP, indicating that predicted results were almost the same as actual values. The process of droplet formation was similar to the one in cell printing (Figs. 3, 4, 5, and 6 in the literature). This suggests that MLP should be also applicable to control droplet formation in cell printing.

In this paper, a learning-based cell injection control (LCIC) method combining MLP with CFD simulation is demonstrated to eliminate satellite droplets automatically to make sure that each droplet with cells can be printed on the specific position. The LCIC method attempts to replace complex theoretical analysis of piezoelectric DOD printing as well as time-consuming and repetitive trial-and-error work at the beginning of DOD printing process. The DOD printing in the study is based on the piezoelectric print-head. CFD simulations, instead of experiments, were used to obtain the datasets for MLP because of its convenience and accuracy, and MLP was selected to optimize the printing process. The LCIC method can thus optimize

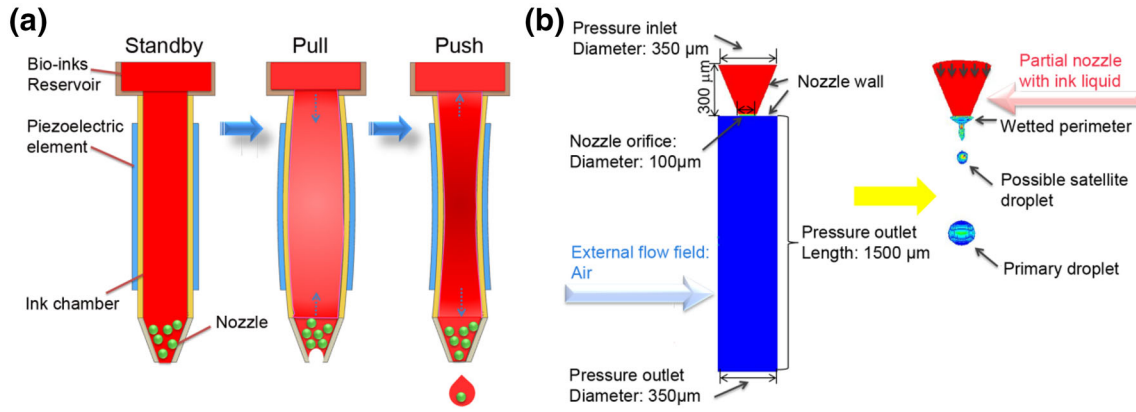


**FIGURE 2.** Schematic and simulation setup of the piezoelectric DOD print-head. (a) Schematic of the piezoelectric DOD print-head. The print-head is comprised of four parts: the bio-ink reservoir, the piezoelectric element, the ink chamber and the nozzle; (b) Simulation setup of the piezoelectric DOD print-head. It comprises a partial print-head with the nozzle (marked in red) and the external air flow field (marked in blue). The inlet of print-head is set as pressure inlet, the nozzle wall is set as wall boundary condition, and the boundary around the external flow is set as pressure outlet. Primary droplet with satellite droplets is simulated with the simulation setup.

DOD cell printing parameters to replace the experimental trial-and-error work for elimination of satellite droplets, providing a good support for subsequent cell printing experiments. Validations of the simulation model and the LCIC method were carried out to demonstrate the feasibility and effectiveness of the demonstrated method.

## MATERIALS AND METHODS

The LCIC approach consists of a specific computational fluid dynamics (CFD) model of piezoelectric DOD print-head to replace experiments, and a multi-layer perceptron (MLP) based on artificial neural network (ANN) algorithm for optimal control of DOD printing.

### Learning-Based Cell Injection Control Method

#### CFD Simulation of the Piezoelectric DOD Print-Head

In piezoelectric DOD printing, a transient mechanical pulse is applied directly to the fluid in the print-head by a piezoelectric actuator based on inverse piezoelectric effect, extruding the bio-ink through the nozzle and producing droplets as shown in Fig. 2(a). At each pulse cycle, a voltage is applied to the piezoelectric ceramic tube of the print-head to deform the wall of the tube. The deformation causes transient changes of internal fluid volume to generate a pressure to produce droplets. Satellite droplets are formed due to Rayleigh instability. They can be suppressed when the viscous force of fluid resists Bernoulli pressure (generated by droplet kinetic energy) and hydrody-

**TABLE 1.** List of symbols.

Symbols	
$\varepsilon$	Deformation displacement of the tube along the thickness direction (m)
$r$	Inner diameter of the piezoelectric ceramic tube (m)
$U$	The applied voltage (V)
$V$	Initial volume of the fluid ( $\text{m}^3$ )
$\Delta V$	The change of fluid volume ( $\text{m}^3$ )
$\Delta p$	Pressure variation (Pa)
$K$	Bulk modulus of elasticity of the fluid. The cell-laden bio-ink is considered to have the same $K$ with water, which is $2.18 \times 10^9$ Pa.
$d_{33}$	The piezoelectric strain constant for PZT-5H, $593 \times 10^{-12} \text{ m V}^{-1}$
$\rho$	Density of the fluid ( $\text{kg m}^{-3}$ )
$\mu$	Viscosity of the fluid ( $\text{kg m}^{-1} \text{ s}$ )
$\alpha$	Volume fraction
$\beta$	Volume-averaged fluid property inside a grid cell
$f^\sigma$	Surface tension (N)
$\bar{\rho}$	Volume-averaged density computed using Eq. (6)
$u$	Velocity ( $\text{m s}^{-1}$ )
Subscripts	
$l$	Liquid phase, i.e., cell-ink in this paper
$g$	Gas phase, i.e., air in this paper
$i$	Current calculated phase in the fluid
$j$	The other phase in the fluid

namic instability (mainly driven by the surface tension).<sup>28,29</sup>

To simulate piezoelectric DOD printing with the CFD model, the liquid phase is regarded as compressible, and the inverse piezoelectric effect is considered in the pressure boundary condition to improve simulation accuracy. The effect of inverse piezoelectric effect combining compressible fluid theory can be expressed as shown in Eqs. (1)–(3). The description of symbols is shown in Table 1. Pressure wave propagation in the print-head causes droplet formation and is

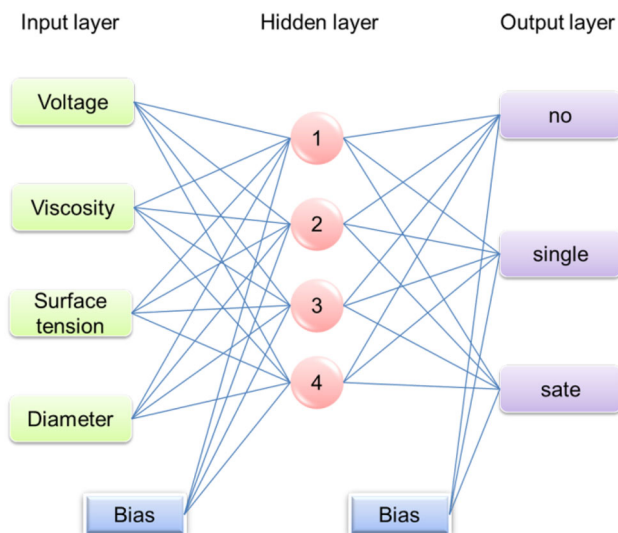


**FIGURE 3.** The MLP designed in this paper. The designed MLP includes three layers: an input layer, a hidden layer and an output layer. The input layer is comprised by four printing parameters, the hidden layer, including four hidden nodes, is used to establish the non-linear system of the designed MLP, and the output layer is used to export the classification results. Biases are the basic parameters of MLP to improve the classification accuracy.

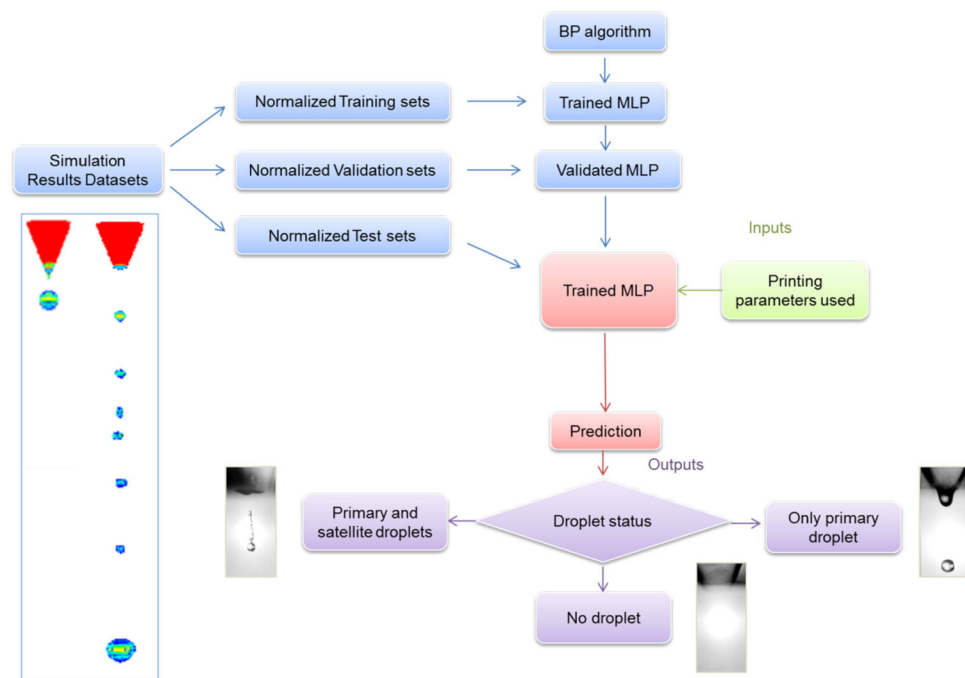


**FIGURE 4.** Schematic of the LCIC method. Datasets are then normalized for building the MLP. The MLP is trained by normalized training sets with BP algorithm and tuned by normalized validation sets. Its performance is assessed by normalized test sets. The trained MLP is used to predict the likely printing outcome with a given input parameter set. The simulation picture shows the primary droplet and the primary droplet with satellite droplets simulated under specific printing parameters.



TABLE 2. Properties of cell-laden bio-ink.

Bio-ink	DMEM	SA (w/v) <sup>a</sup>	Cell (mL <sup>-1</sup> ) <sup>a</sup>	Density (g mL <sup>-1</sup> )	Viscosity (cP)	Surface tension (mN m <sup>-1</sup> )
A	Yes	0	1 × 10 <sup>6</sup>	1.00	1.0 <sup>14</sup>	72.19 <sup>14</sup>
B	No	0.5%	1 × 10 <sup>6</sup>	0.989 <sup>10</sup>	5.0 <sup>20</sup>	71.00 <sup>18</sup>
C	No	1.0%	0.5 × 10 <sup>6</sup>	0.989 <sup>10</sup>	10.0 <sup>20</sup>	70.03 <sup>17</sup>

<sup>a</sup>SA and Cell in table refer to SA concentration and cell concentration respectively.

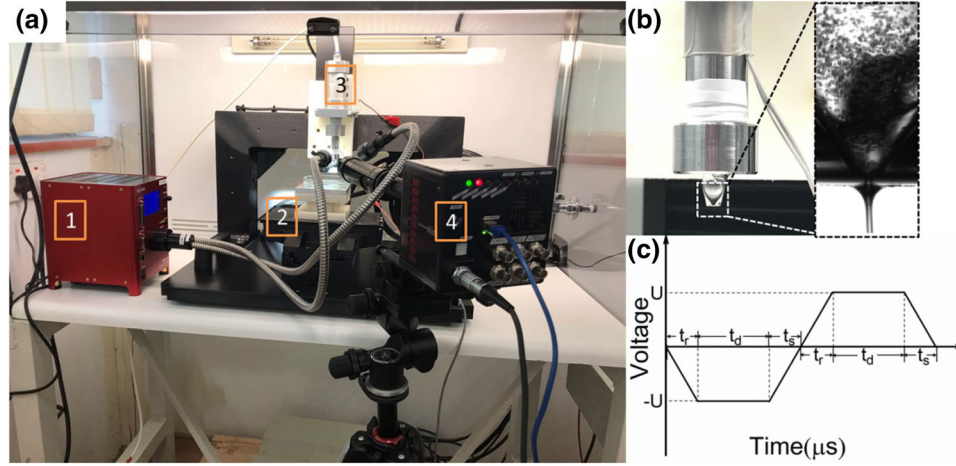


FIGURE 5. (a) Experimental setup of piezoelectric DOD cell printing. 1—super bright LED; 2—3D working platform; 3—the in-house-developed piezoelectric DOD print-head; 4—high-speed camera; (b) Magnification of the DOD print-head and Hela cells bio-ink in the glass nozzle of the print-head; (c) Schematic of the bipolar voltage pulse wave.  $t_d$  the dwell time,  $t_r$  the rise time,  $t_f$  the fall time.

approximated according to Eqs. (1)–(3) and the theory of acoustic wave.<sup>3</sup>

$$\varepsilon = d_{33}U \quad (1)$$

$$\frac{\Delta V}{V} = \frac{\varepsilon}{r} \quad (2)$$

$$\Delta p = -K \frac{\Delta V}{V} \quad (3)$$

Figure 2(b) shows the simulation setup of the piezoelectric DOD print-head. The part in red simulates a partial print-head with the nozzle.  $\Delta p$ , defined by Eq. (3), is the pressure boundary for the pressure inlet. The external flow field, marked in blue in the figure, is used to observe droplets formation and movement. The pressure outlet boundary condition is used on the boundary around the external flow and a no-slip boundary is used for simulating the nozzle wall.

Continuity equation (Eq. 4) and Navier–Stokes equation (Eq. 5), along with the inverse piezoelectric effects (Eqs. 1–3), form a complete mathematical description for the gas–liquid two-phase flow problem of the piezoelectric DOD printing. The corresponding CFD model was developed on ANSYS FLUENT to

simulate the printing process. Considering that the volume fraction of cells in the bio-ink is quite small (0.419% for 10<sup>6</sup> cells mL<sup>-1</sup> cell-laden bio-ink), influence of cells on bio-ink can be ignored. Hence, droplet formation is treated as a pseudo-two-phase flow (bio-ink as a liquid phase, and the air outside the print-head as a gas phase) during the simulation. The volume-of-fluid (VOF) model in Eq. (6) is used to simulate droplet formation and continuum surface force (CSF) model in Eq. (7) is selected as the surface tension model.<sup>4</sup> The 3D transient pressure-based solver is used for solving the simulation model, in which the fluid is simulated by laminar flow model and the wall boundary is built by standard wall functions. For computational stability, a Pressure-Implicit with Splitting of Operators (PISO) pressure–velocity coupling scheme is adopted to solve governing formulations. Second order Upwind Difference Scheme (UDS) is adopted to improve computational accuracy; meanwhile, geometric reconstruction scheme is applied to track the interface between fluid phases using a piecewise linear approach.<sup>9</sup> The time step in simulation is set as an adaptive variant to avoid simulation distortion by ensuring the Courant number not exceeding 0.8. The tolerance of each governing equation is set as

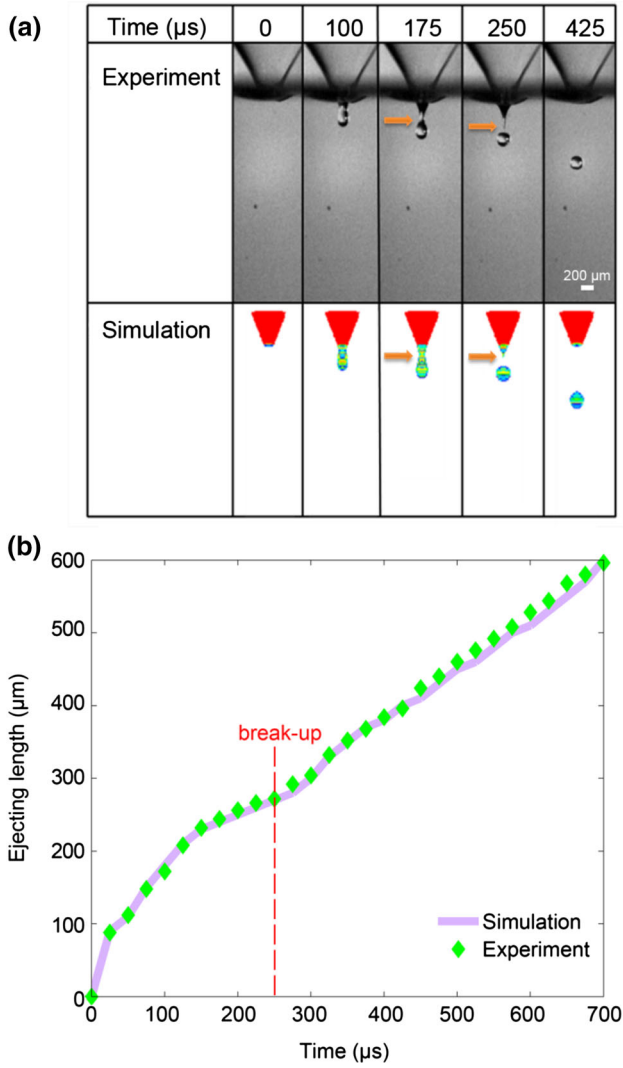


**FIGURE 6.** Experimental validations of the CFD simulation. (a) Formation of an ejected ink droplet obtained by the high-speed camera and CFD simulation; (b) Ejecting length of the droplet with measurement and simulation. \*Arrows indicate the ink column is sucked back into the nozzle gradually.

$10^{-6}$  to keep the computational error within an acceptable range.

$$\frac{\partial \rho}{\partial t} + \nabla \cdot (\rho \mathbf{u}) = 0 \quad (4)$$

$$\frac{\partial}{\partial t} (\rho \mathbf{u}) + \nabla \cdot (\rho \mathbf{u} \mathbf{u}) = -\nabla p + \nabla \cdot [\mu (\nabla \mathbf{u} + \nabla \mathbf{u}^T)] + \mathbf{f}^\sigma \quad (5)$$

$$\beta = (1 - \alpha)\beta_l + \alpha\beta_g \quad (6)$$

$$\mathbf{f}_i^\sigma = -\sigma \frac{\bar{\rho} \nabla \frac{\alpha_i}{|\mathbf{x}_i|} \nabla \alpha_i}{\frac{1}{2}(\rho_i + \rho_j)} \quad (7)$$

### Artificial Neural Network (ANN)

Artificial neural networks are biologically-inspired machine learning algorithms, designed to mimic behaviors and characteristics of neural networks in the biological brain. The Multilayer Perceptron (MLP) is a class of ANNs. It consists of three types of layers—input layer, hidden layers and output layer,<sup>21</sup> as shown in Fig. 3. Parameters to be analyzed constitute the input layer, and classification results are exported by the output layer. Middle hidden layers between them establish the non-linear classification system. The number of hidden layers can be one or many.

To obtain a satisfactory MLP with high classification accuracy, weights used in the processing element are trained with a learning rule. The learning procedure was carried out with the back propagation algorithm (BP).<sup>21</sup> Every weight in the network is updated incrementally with the appearance of new training sample  $x_{ji}$  in Eqs. (8a) and (8b).

$$w_{ji}(n+1) = w_{ji}(n) + \Delta w_{ji}(n) \quad (8a)$$

$$\Delta w_{ji}(n) = \beta \delta_j x_{ji} + \alpha \Delta w_{ji}(n-1) \quad (8b)$$

In Eq. (8b),  $\beta$  is learning rate, determining the convergence rate of weights,  $j$  and  $i$  represent the nodes of different layers, and  $\beta \delta_j x_{ji}$  is the weight updated formula of BP algorithm.  $\alpha \Delta w_{ji}(n-1)$  is the improvement item of BP to smooth the search process of optimum, called momentum item, where  $\alpha$  is momentum coefficient. Through varying learning rate and momentum coefficient, the MLP performance can be changed.

MLP structure is commonly determined by numbers of hidden layers as well as hidden nodes. Inappropriate numbers of hidden layers or nodes will result in a reduction in prediction accuracy. It was shown that one hidden layer was available to fit any continuous function with very high accuracy.<sup>19</sup> As such, only the number of hidden nodes, termed as ‘H’, would be optimized.

### Scheme of the LCIC Method

The demonstrated LCIC method is shown in Fig. 4. CFD simulations are carried out to obtain datasets for development of the MLP. Datasets are divided into three categories: training sets, validation sets, and test sets. Training sets are used to train the MLP, validation sets are used to tune the MLP parameters for the minimization of over-fitting, and test sets are used to assess the performance of MLP. Through the learning process, the MLP would be able to predict, based on

given input parameter set, the likely outcome of the printing.

Printing parameters in this system are voltage, diameter of the nozzle, bio-ink viscosity and surface tension. These four parameters have direct influence on droplet formation and hence are set as inputs. Outputs of MLP are termed as three labels: 'no', 'yes' and 'sate', representing no droplets, only primary droplet and both of primary and satellite droplets, respectively. The structure of the network is set to 4: H: 3 (input nodes: hidden nodes: output nodes).

Using the developed MLP, a printing outcome could be predicted when values of printing parameters are entered.

#### *Experimental Setup for Validation of the Simulation Model and LCIC Method*

##### *Cell-Laden Bio-Ink Preparation*

HeLa is a popular cell line in scientific research with an average density of  $1.06 \text{ g mL}^{-1}$ .<sup>16</sup> HeLa cell (Lonza) culture was performed with high glucose Dulbecco's Modified Eagle Medium (DMEM) with 1% penicillin, under  $37^\circ\text{C}$  in an atmosphere of 5%  $\text{CO}_2$  incubator. DMEM and penicillin were obtained from Invitrogen Singapore. Cells were separated from the flask with 0.25% trypsin-EDTA and suspended in DMEM to prepare cell suspension for bio-ink. The diameter of HeLa in suspension was measured as  $18 \mu\text{m}$  through Tali<sup>®</sup> Image-Based Cytometer (Thermo Fisher Scientific, USA), and the cell concentration was  $1 \times 10^6 \text{ mL}^{-1}$ . To investigate the correctness of our LCIC method, HeLa cells were also suspended in sodium alginate (SA). Properties of cell-laden bio-ink are shown in Table 2.

##### *Setup of Piezoelectric DOD Cell Printing and High-Speed Camera System*

An in-house-developed piezoelectric DOD print-head<sup>14</sup> with a nozzle diameter of  $100 \mu\text{m}$  was used in this study (Fig. 5a). A high-speed camera (Mini AX200 model, Photron), assisted by a super bright LED (SLG-150V, REVOX Solutions by Photron), was used to capture the droplet trajectory at 40,000 frame rate. The camera was focused on the middle plane of the nozzle, and the droplet formation process was recorded. Figure 5b shows magnification of the DOD print-head and HeLa cells bio-ink in the glass nozzle of the printer. The black part in the center of image was a defect on the outside wall of nozzle, which was broken accidentally during the experiment. Nevertheless, it had no influence on experimental results.

During the cell printing process, the cell suspension was first supplied in the print-head. A negative pres-

sure was then generated by an air compressor (Sil Air 30HA, SilentAire). A pressure regulator (AD 3000D, Iwashita Engineering, Inc) was used to adjust the negative pressure to balance the gravity of cell-suspended bio-ink, preventing the leakage of ink from the orifice. A bipolar wave type of voltage pulse, as shown in Fig. 5c, was applied to a piezo driver (JetDrive<sup>TM</sup> III, Microfab Technologies Inc.), which was connected with the transducer of the print-head. The pulse frequency was 100 Hz, the dwell time ( $t_d$ ) was  $300 \mu\text{s}$  and the rise time ( $t_r$ ) and the fall time ( $t_f$ ) were both  $3 \mu\text{s}$ . At each pulse, the internal ink was squeezed to generate droplets. Cell-suspended bio-ink was printed on dry cell culture planes, and an optical microscopy (Olympus BX41) was utilized to observe their deposition.

## RESULTS

#### *Applied Voltage Range and Validation of the Simulation Model*

The voltage in the simulation of the DOD print-head was set at equal or more than 27 V because droplets cannot be ejected in experiments with a voltage smaller than 27 V. Detailed discussion was described in supplementary materials. Experimental data were calculated as the mean value of measured results on ten groups of pictures obtained by the high-speed camera. The time before bio-ink is pushed out of the nozzle was set to zero.

As shown in Fig. 6(a), at  $t = 100 \mu\text{s}$ , the bio-ink meniscus was pushed out of nozzle under the positive voltage applied on the PZT-5H ceramic tube. At  $t = 175 \mu\text{s}$ , the ink column was sucked back to the nozzle gradually as indicated by the arrow and finally broke up into a free droplet, at  $t = 250 \mu\text{s}$ . The droplet shape was changed by vibration continually and finally stabilized in sphere shape, at  $t = 425 \mu\text{s}$ . Simulation and experiments matched well on the droplet formation process from extruding bio-ink out to the break-up of droplet. The diameter of droplet in simulation and experiment was 117.5 and  $110 \mu\text{m}$  respectively, with the error of 6.82%.

The ejecting length of bio-ink in simulation also agrees very well with the experimental ones (Fig. 6b). Before the bio-ink breaking into a droplet, at  $t = 100 \mu\text{s}$  and  $t = 175 \mu\text{s}$ , the error of ejecting length between simulations and experiments is 2.1 and 1.6%, respectively. The maximum error before the break-up of droplet is 2.3%. When the bio-ink broke up into the droplet, at  $t = 250 \mu\text{s}$ , the error is 0.7%. After droplets breaking, droplet positions from the nozzle in simulation are slightly higher than those of the experiments. The maximum error is 4%. The error gener-

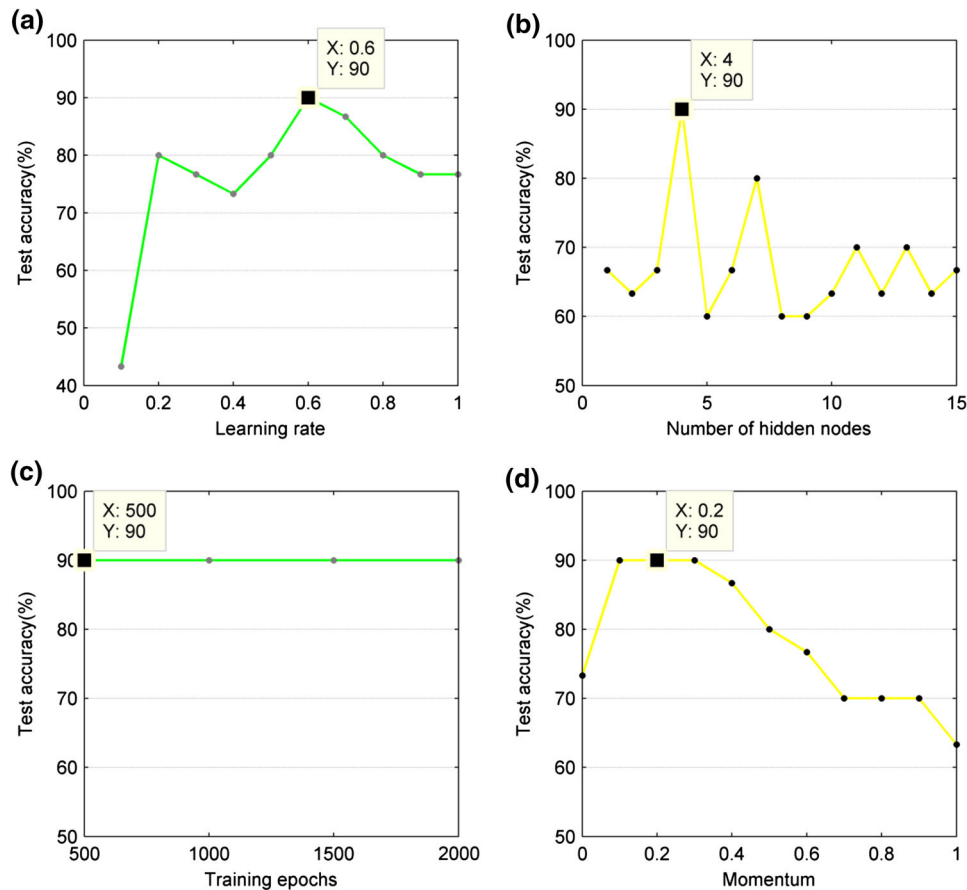


**FIGURE 7. Test accuracy of the MLP. (a) Testing accuracy vs. learning rate for classification; (b) Testing accuracy vs. hidden nodes for classification; (c) Testing accuracy vs. training epochs for classification; (d) Testing accuracy vs. momentum for classification.**

ated in simulation is mainly due to the ignorance of cells influence. Cells in the droplet are not homogeneously distributed but tends to strongly attach to the interface.<sup>28</sup> The surface tension of bio-ink during ejecting is decreased, which is beneficial to increase droplet speed. Overall, the demonstrated simulation model matched reasonably well with experiments on the droplet formation during piezoelectric DOD printing. It can be used to simulate different droplet statuses generated under various printing parameters, including satellite droplets.

#### *MLP Performance*

The MLP algorithm was developed on Matlab. A total of 99 simulation results were obtained as datasets for the MLP, of which 59 were used as training sets, 10 as validation sets, and 30 as test sets. In inputs of dataset, the range of voltages was 27–57 V; the range of viscosity was 1.07–20 cP; the range of surface tension was 38–72.19 mN m<sup>-1</sup>; and the range of nozzle diameter was 25–120  $\mu$ m. Ranges of voltage and vis-

cosity were set according to the working scope of our DOD print-head,<sup>14</sup> the range of surface tension was set considering common cell concentrations of the bioink,<sup>28</sup> and the range of nozzle diameter was set to make sure that it is larger than the diameter of cells commonly used for bioprinting. Values of each input are selected randomly, which are described in supplementary materials. Outputs of dataset include: 'no', 'yes' and 'sate', representing no droplets, primary droplet, and primary and satellite droplets, respectively. The highest self-learning performance of MLP was achieved through the adjustment of four major factors namely learning rate, number of hidden nodes, training time and momentum.

Learning rate was used to reduce the error between the target value and the actual value. Initially, the number of hidden nodes was set as four, the training time was set as 500 and the momentum was set as 0.2. Figure 7a shows the analysis of learning rate, where the highest test accuracy of 0.6 was obtained. When the learning rate was larger than 0.6, the network failed to achieve the best performance because of over-fitting.



Thus the learning rate was selected as 0.6 for the following analysis of the learning rate.

Hidden node is one of the most important structure parameters of the MLP. Based on the results in Fig. 7b, the best classification performance is obtained with four hidden nodes at a testing accuracy of 90.00%. For 1–3 hidden nodes, the underfitting structure of MLP causes the prediction accuracy to be lower than 70%. As the number of hidden nodes was changed from 3 to 4, the prediction accuracy was increased to the highest test accuracy from 66.67 to 90.00%. When the number of hidden nodes was set larger than 4, over-fitting was observed and thus the test accuracy was decreased. Therefore, four hidden nodes network was chosen as the optimal parameter.

Optimal parameters obtained above were used for the analysis of training time with the test range from 500 to 2000, shown in Fig. 7c. Results showed that the test accuracy is 90.00% without variation when changing the size of training epochs, which demonstrates the network was fully trained. Figure 7d shows the optimization of momentum, at which the best value of momentum is from 0.1 to 0.3. If the momentum was not added in the MLP (i.e., momentum = 0.0), the weights cannot get rid of local optimum for global optimum. When the momentum is larger than 0.3, the weights deviated from the global optimum and caused the decrease of test accuracy of MLP performance. As a result, the momentum was set as 0.2.

The results indicate that MLP with one hidden layer and four hidden nodes, 0.6 learning rate, 500 training epochs and 0.2 momentum has good classification performance with test accuracy of 90.00%.

#### *Experiment Validation of LCIC Method*

User interface of the developed MLP is shown in Fig. 8a. Four sets of input parameters were entered in the columns called 'Inputs' and the results were presented in the columns called 'Predictions'. Distance between the DOD print-head and the substrate was set as 10 mm in experiments to prevent producing splash droplets. Based on voltage amplitudes chosen randomly in two sets of experiments (30, 58 and 68 V in first set and 28, 29 and 43 V in second set), results of the LCIC method are shown in Table 3, which matched well with experimental results (Figs. 8b and 8d). In first set, the speed of 3D platform was  $20 \text{ mm s}^{-1}$ . Bio-ink B and C were used in experiments. Stable primary droplet was produced by the first group parameters, i.e., the voltage of 30 V, the viscosity of 5 cP, the surface tension of  $71 \text{ mN m}^{-1}$  and the nozzle diameter of  $100 \mu\text{m}$ , matching with the result of 'yes'. No droplets were printed under the second group of parameters, matching with the result of 'no', and satellite

droplets were generated with the third and fourth group of parameters, matching with the result of 'sate'. In second set, the speed of 3D platform is  $30 \text{ mm s}^{-1}$ . Bio-ink A was used in experiments. Stable primary droplet was produced by both of the fifth and sixth group of parameters, matching with 'yes' in LCIC results. Satellite droplets were generated with the last group parameters, matching with the result of 'sate'. After printing on the substrate, the arrays of droplets encapsulating cells are shown in Figs. 8c and 8e.

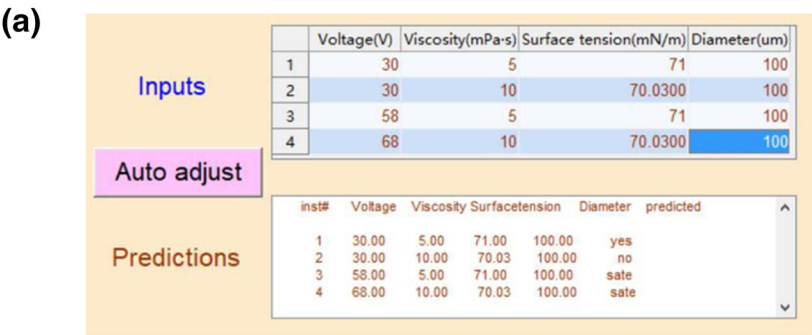
## DISCUSSIONS

### *Cell Printing Patterns Using LCIC Method*

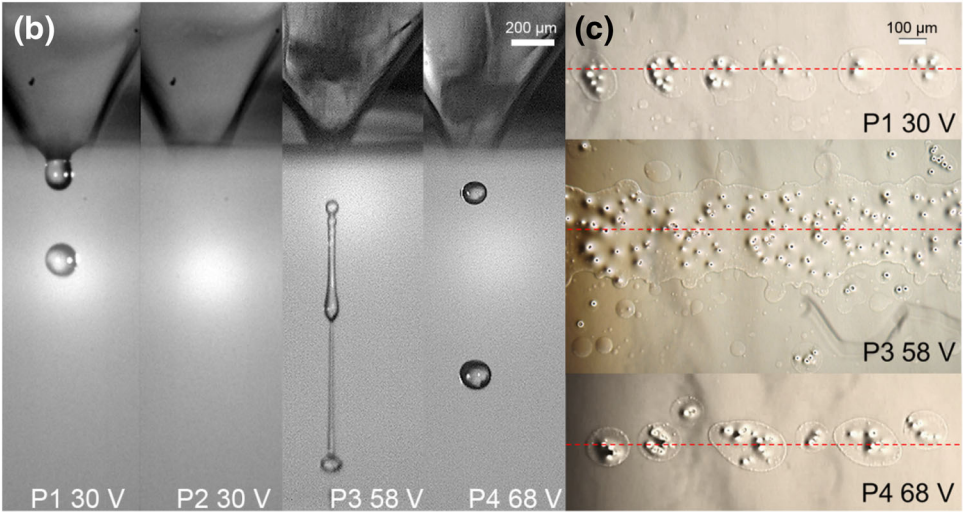
The demonstrated LCIC method can help print droplets encapsulating cells without satellite droplets on the designed position rapidly and conveniently for creation of organized constructs based on the accurate prediction performance. In first set of experiments (Fig. 8b), when satellite droplets were eliminated (labelled by 'P1 30V'), the single droplet with encapsulating cells was printed orderly in the specified line (marked as red dash line). The distance between each droplet was homogenous and could be controlled by changing the speed of 3D platform. This is the ideal performance for printing cells with bio-ink. On the contrary, printing a primary droplet with satellite droplets would show a disordered cells array. When too much satellite droplets generated (labelled by 'P3 58V'), the printed line of cells was two times wider than the ideal one, compassed with splashed cells. As a result, the printing resolution was decreased, impairing the advantage of DOD printing. When the size of satellites droplets are small (labelled by 'P4 68V'), the printed satellite droplets are still uncontrollably, such as the third droplet and the fifth droplet from the left (Fig. 8d), causing the distance between droplets inhomogeneous. The significance of droplet status is more obvious in the second set of experiments. When the single droplet was printed (labeled by 'P5 28V', 'P6 29V'), the size and the distance between droplets was uniform. Compared experiments labeled by 'P7 43V' and 'P6 29V', the distance between droplets in 'P7 43V' was half of the one in 'P6 29V' while the width of the printed line in 'P7 43V' was three times larger than the one in 'P6 29V'. Cells deviating from specific distribution may cause errors on future cell function and tissue structure.<sup>26</sup>

### *Features of LCIC Method*

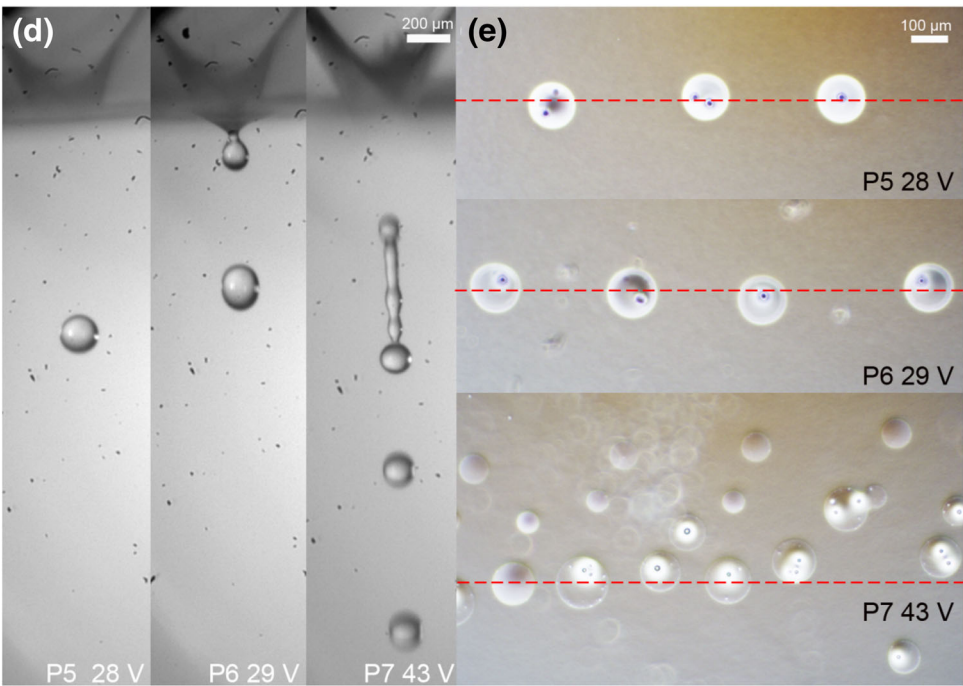
In the LCIC method, data of droplet formation are generated by simulations. The relationship between



I . First set of experiments



II . Second set of experiments



◀ **FIGURE 8.** Experimental results for validation of the LCIC method. P means Predictions. (a) User interface of the developed MLP. (b–c) First set of experiments: Bio-ink B and C are used. The speed of 3D platform is 20 mm s<sup>-1</sup>; (b) Droplets with encapsulating cells printed; (c) Droplets with encapsulating cells printed on the substrate; (d–e) Second set of experiments: Bio-ink A is used. The speed of 3D platform is 30 mm s<sup>-1</sup>. (d) Droplets with encapsulating cells printed; (e) Droplets with encapsulating cells printed on the substrate. Only primary droplets are generated in P1, P5, and P6 groups, no droplet is generated in P2 group, and both primary and satellite droplets are generated in P3, P4, and P7 groups. Red dash line is the planning route.

droplet formation status and printing parameters are analysed by the developed MLP, replacing the repetitive trial-and-error process.

Several studies<sup>13,23</sup> on CFD simulation have been conducted to study the printability of inks and characteristics of droplets with empirically setting of a specified pressure or velocity as the boundary condition of the nozzle inlet. However, these simulations need trial-and-errors to match experimental results. The reason is that the pressure or velocity used in simulation is an indirect parameter and their relationship with actual printing parameters is not clear. In this paper, this research gap is solved by adding the corresponding piezoelectric mathematical model into the simulation model to integrate the mathematical model of piezoelectric DOD printing for improvement of the simulation accuracy.

According to the description in Sect. “Artificial Neural Network (ANN)” and the theory,<sup>21</sup> the developed MLP is a kind of non-linear models, as shown in Eq. (9).

$$Y = \text{sigmoid}(\text{sigmoid}(X \cdot w_1 + b_1) \cdot w_2 + b_2) \quad (9)$$

where  $Y$  is a  $1 \times 3$  outputs matrix as the label of classification, and the value is classification probability;  $X$  is a  $1 \times 4$  normalization of inputs matrix, including voltage, viscosity, surface tension and nozzle diameter; sigmoid is the active function of MLP,<sup>21</sup>  $w_1$  and  $b_1$ ,  $w_2$  and  $b_2$  are weights and bias in the hidden

layer and the outputs layer, respectively. Values of  $w_1$ ,  $b_1$ ,  $w_2$ , and  $b_2$  can be found in supplementary materials.

Normalization is used to eliminate the effect caused by different magnitudes of parameter values. For instance, the voltage value is several tenfold higher than the viscosity value. Each normalized value of printing parameters  $x_i$  can be solved by Eq. (10).

$$x'_i = \frac{x_i - (\max + \min)/2}{(\max - \min)/2} \quad (10)$$

where  $x$  is the value of printing parameters, and  $\max$  and  $\min$  are the maximum and minimum value of each printing parameters in training data.

LCIC method is demonstrated mainly for optimizing the droplet status printed by our piezoelectric DOD print-heads. Nevertheless, it can be adjusted for optimization of other print-heads with the same actuation mode of piezo-ceramic tube. Among four input parameters of the LCIC method, the pressure generated by the applied voltage with different printers might be discriminative due to various structural parameters. The applied voltages should be scaled based on Eqs. (1)–(3) with LCIC method.

Machine learning technology has been applied in many fields and was proved to be good for classification.<sup>7,24</sup> In this study, it has been proved that the developed MLP based on ANN algorithm is good for optimal control of piezoelectric DOD printing. Test accuracy of the MLP developed is 90.00% as mentioned before. Since there is still 10% error of the developed MLP, further studies could be carried out to reduce the error for improving accuracy of the developed MLP.

Moreover, LCIC method can be used to replace the time-consuming and repetitive trial-and-error process of DOD cell printing. In previous DOD printing experiments, the printer is usually adjusted manually. There are two problems in this process. First, if the printer cannot work, the trial-and-error process has to be carried out. Second, satellite droplets are too small to be observed. It might need high speed camera for observing

**TABLE 3.** Results of LCIC method.

Group no.	Voltage (V)	Viscosity (cP)	Surface tension (mN m <sup>-1</sup> )	Diameter (μm)	Droplet status
First set of experiments					
P1	30	5	71	100	Yes
P2	30	10	70.03	100	No
P3	58	5	71	100	Sate
P4	68	10	70.03	100	Sate
Second set of experiments					
P5	28	1	72.19	100	Yes
P6	29	1	72.19	100	Yes
P7	43	1	72.19	100	Sate

In first set of experiments: the speed of 3D platform is 20 mm s<sup>-1</sup>; In second set of experiments: the speed of 3D platform is 30 mm s<sup>-1</sup>.



satellite droplets;<sup>27</sup> however, the experimental expense is costly as well. While LCIC method is developed as a non-linear model of piezoelectric DOD printing, it can help users to predict droplet statuses with the input printing parameters. The time of adjustment can be reduced from hours to a few seconds.

## CONCLUSION

In this paper, the LCIC method combining of CFD simulation and MLP is demonstrated to eliminate satellite droplets by automatically adjusting piezoelectric DOD printing in cell printing. The LCIC method comprises a specific CFD model of piezoelectric DOD print-head to replace experiments, and an MLP to optimize DOD printing parameters. 99 simulation results in total based on voltage, bio-ink viscosity and surface tension coefficient and nozzle diameter were obtained for the development of the MLP. Results show that the MLP comprising one hidden layer with four hidden nodes, 0.6 learning rate, 500 training epochs and 0.2 momentum has good classification performance with the test accuracy of 90.00%. Precise cell patterns can be achieved through implementation of the LCIC method in experiments. Compared with the time-consuming and repetitive trial-and-error process, the LCIC method can be used to automatically complete DOD cell printing parameters optimization with the replace of manual expense in a few seconds, which improves the efficiency dramatically.

This paper mainly focuses the LCIC method performance in the low viscosity range in DOD cell printing. It can also be improved to adjust printing performance with high viscosity bio-ink by training the MLP with relevant datasets. It has shown huge potential to apply machining learning to reduce trial-and-error work and to improve manufacturing precision in cell printing. In further research, we will discuss the influence of the droplet speed and droplet size on cell printing precision and optimize droplet characteristics with the LCIC method. The LCIC method will also be used to optimize the print-head structure and corresponding printing parameters to design a widely applicable and easily adjusted printing system for common bio-ink.

## ACKNOWLEDGMENT

Jia Shi thanks the China Scholarship Council (CSC) for the financial support of a visiting program at National University of Singapore.

## CONFLICT OF INTEREST

The authors declare that they have no financial or personal relationships with other people or organizations that could inappropriately have influenced their work.

## REFERENCES

- <sup>1</sup>Ahlfeld, T., A. R. Akkineni, Y. Förster, T. Köhler, S. Knaack, M. Gelinsky, and A. Lode. Design and fabrication of complex scaffolds for bone defect healing: combined 3D plotting of a calcium phosphate cement and a growth factor-loaded hydrogel. *Ann. Biomed. Eng.* 45:224–236, 2017.
- <sup>2</sup>Barron, V., K. Merghani, G. Shaw, C. Coleman, J. Hayes, S. Ansboro, A. Manian, G. O'Malley, E. Connolly, and A. Nandakumar. Evaluation of cartilage repair by mesenchymal stem cells seeded on a PEOT/PBT scaffold in an osteochondral defect. *Ann. Biomed. Eng.* 43:2069–2082, 2015.
- <sup>3</sup>Bogy, D. B., and F. Talke. Experimental and theoretical study of wave propagation phenomena in drop-on-demand ink jet devices. *IBM J. Res. Dev.* 28:314–321, 1984.
- <sup>4</sup>Brackbill, J., D. B. Kothe, and C. Zemach. A continuum method for modeling surface tension. *J. Comput. Phys.* 100:335–354, 1992.
- <sup>5</sup>Dey, R., A. Ghoshal, and B. Tudu. Electromyogram (EMG) signal categorization in parkinson's disease tremor detection by applying MLP (Multilayer Perceptron) technique: a review. *Advances in Systems, Control and Automation*, Singapore: Springer, 2018, pp. 693–699.
- <sup>6</sup>Dhanarajan, G., M. Mandal, and R. Sen. A combined artificial neural network modeling–particle swarm optimization strategy for improved production of marine bacterial lipopeptide from food waste. *Biochem. Eng. J.* 84:59–65, 2014.
- <sup>7</sup>Dos Santos, E. B., R. Pistor, and A. P. Gerlich. Pulse profile and metal transfer in pulsed gas metal arc welding: droplet formation, detachment and velocity. *Sci. Technol. Weld. Join.* 22:627–641, 2017.
- <sup>8</sup>Dudhagara, D. R., R. K. Rajpara, J. K. Bhatt, H. B. Gosai, and B. P. Dave. Bioengineering for polycyclic aromatic hydrocarbon degradation by *Mycobacterium litorale*: Statistical and artificial neural network (ANN) approach. *Chemometrics Intell. Lab. Syst.* 159:155–163, 2016.
- <sup>9</sup>Fluent, A. 14.5, theory guide. Canonsburg: Ansys Inc., 2012.
- <sup>10</sup>Hatami, M., and D. Ganji. Natural convection of sodium alginate (SA) non-Newtonian nanofluid flow between two vertical flat plates by analytical and numerical methods. *Case Stud. Thermal Eng.* 2:14–22, 2014.
- <sup>11</sup>Kani, M. H., E. C. Chan, R. C. Young, T. Butler, R. Smith, and J. W. Paul. 3D cell culturing and possibilities for myometrial tissue engineering. *Ann. Biomed. Eng.* 45:1746–1757, 2017.
- <sup>12</sup>Kotsiantis, S. B., I. Zaharakis, and P. Pintelas. Supervised machine learning: A review of classification techniques. In: *Emerging Artificial Intelligence Applications in Computer Engineering*, edited by R. Mizoguchi, M. Musen, N. Zhong, J. Breuker, R. Dieng-Kuntz, N. Guarino, J. N. Kok, and J. Liu. Amsterdam: IOS Press, 2007, pp. 3–24.



- <sup>13</sup>Lai, J. M., C. Y. Huang, C. H. Chen, K. Linliu, and J. D. Lin. Influence of liquid hydrophobicity and nozzle passage curvature on microfluidic dynamics in a drop ejection process. *J. Micromech. Microeng.* 20:015033, 2010.
- <sup>14</sup>Li, E. Q., Q. Xu, J. Sun, J. Y. H. Fuh, Y. S. Wong, and S. T. Thoroddsen. Design and fabrication of a PET/PTFE-based piezoelectric squeeze mode drop-on-demand inkjet printhead with interchangeable nozzle. *Sens. Actuator A Phys.* 163:315–322, 2010.
- <sup>15</sup>Malda, J., J. Visser, F. P. Melchels, T. Jungst, W. E. Hennink, W. J. Dhert, J. Groll, and D. W. Huttmacher. 25th anniversary article: Engineering hydrogels for bio-fabrication. *Adv. Mater.* 25:5011–5028, 2013.
- <sup>16</sup>Milo, R., and R. Phillips. *Cell Biology by the Numbers*. Abington: Garland Science, 2015.
- <sup>17</sup>Moon, S., B. Y. Ryu, J. Choi, B. Jo, and R. J. Farris. The morphology and mechanical properties of sodium alginate based electrospun poly (ethylene oxide) nanofibers. *Polym. Eng. Sci.* 49:52–59, 2009.
- <sup>18</sup>Muthamizhi, K., P. Kalaichelvi, S. T. Powar, and R. Jaishree. Investigation and modelling of surface tension of power-law fluids. *RSC Adv.* 4:9771–9776, 2014.
- <sup>19</sup>Nasir, A. A., M. Y. Mashor, and H. Rosline. Classification of acute leukaemia cells using multilayer perceptron and simplified fuzzy ARTMAP neural networks. *Int. Arab J. Inf. Technol.* 10:356–364, 2013.
- <sup>20</sup>Nishiyama, Y., M. Nakamura, C. Henmi, K. Yamaguchi, S. Mochizuki, H. Nakagawa, and K. Takiura. Development of a three-dimensional bioprinter: construction of cell supporting structures using hydrogel and state-of-the-art inkjet technology. *J. Biomech. Eng. Trans.* 131:35, 2009.
- <sup>21</sup>Riedmiller, M. Advanced supervised learning in multi-layer perceptrons—from backpropagation to adaptive learning algorithms. *Comput. Stand. Interfaces.* 16(3):265–278, 1994.
- <sup>22</sup>Ross, S. E., Z. Ouyang, S. Rajagopalan, and T. M. Bruns. Evaluation of decoding algorithms for estimating bladder pressure from dorsal root ganglia neural recordings. *Ann. Biomed. Eng.* 46:233–246, 2018.
- <sup>23</sup>Suh, Y., and G. Son. A sharp-interface level-set method for simulation of a piezoelectric inkjet process. *Numer. Heat Transf. B Fundam.* 55:295–312, 2009.
- <sup>24</sup>Tsinalis, O., P. M. Matthews, and Y. Guo. Automatic sleep stage scoring using time-frequency analysis and stacked sparse autoencoders. *Ann. Biomed. Eng.* 44:1587–1597, 2016.
- <sup>25</sup>Vatankhah, E., D. Semnani, M. P. Prabhakaran, M. Tadayon, S. Razavi, and S. Ramakrishna. Artificial neural network for modeling the elastic modulus of electrospun polycaprolactone gelatin scaffolds. *Acta Biomater.* 10:709–721, 2014.
- <sup>26</sup>Wust, S., R. Muller, and S. Hofmann. Controlled positioning of cells in biomaterials-approaches towards 3D tissue printing. *J. Funct. Biomater.* 2:119–154, 2011.
- <sup>27</sup>Xu, C., W. Chai, Y. Huang, and R. R. Markwald. Scaffold-free inkjet printing of three-dimensional zigzag cellular tubes. *Biotechnol. Bioeng.* 109:3152–3160, 2012.
- <sup>28</sup>Xu, C., M. Zhang, Y. Huang, A. Ogale, J. Fu, and R. R. Markwald. Study of droplet formation process during drop-on-demand inkjetting of living cell-laden bioink. *Langmuir* 30:9130–9138, 2014.
- <sup>29</sup>Yang, Q., H. Li, M. Li, Y. Li, S. Chen, B. Bao, and Y. Song. Rayleigh instability-assisted satellite droplets elimination in inkjet printing. *ACS Appl. Mater. Interfaces* 9(47):41521, 2017.
- <sup>30</sup>Zhang, Y., Y. Sun, P. Phillips, G. Liu, X. Zhou, and S. Wang. A multilayer perceptron based smart pathological brain detection system by fractional Fourier entropy. *J. Med. Syst.* 40:173, 2016.